Volume 55 | Number 99 | 25 December 2019 | Pages 14859–15008

ChemComm

Chemical Communications

rsc.li/chemcomm

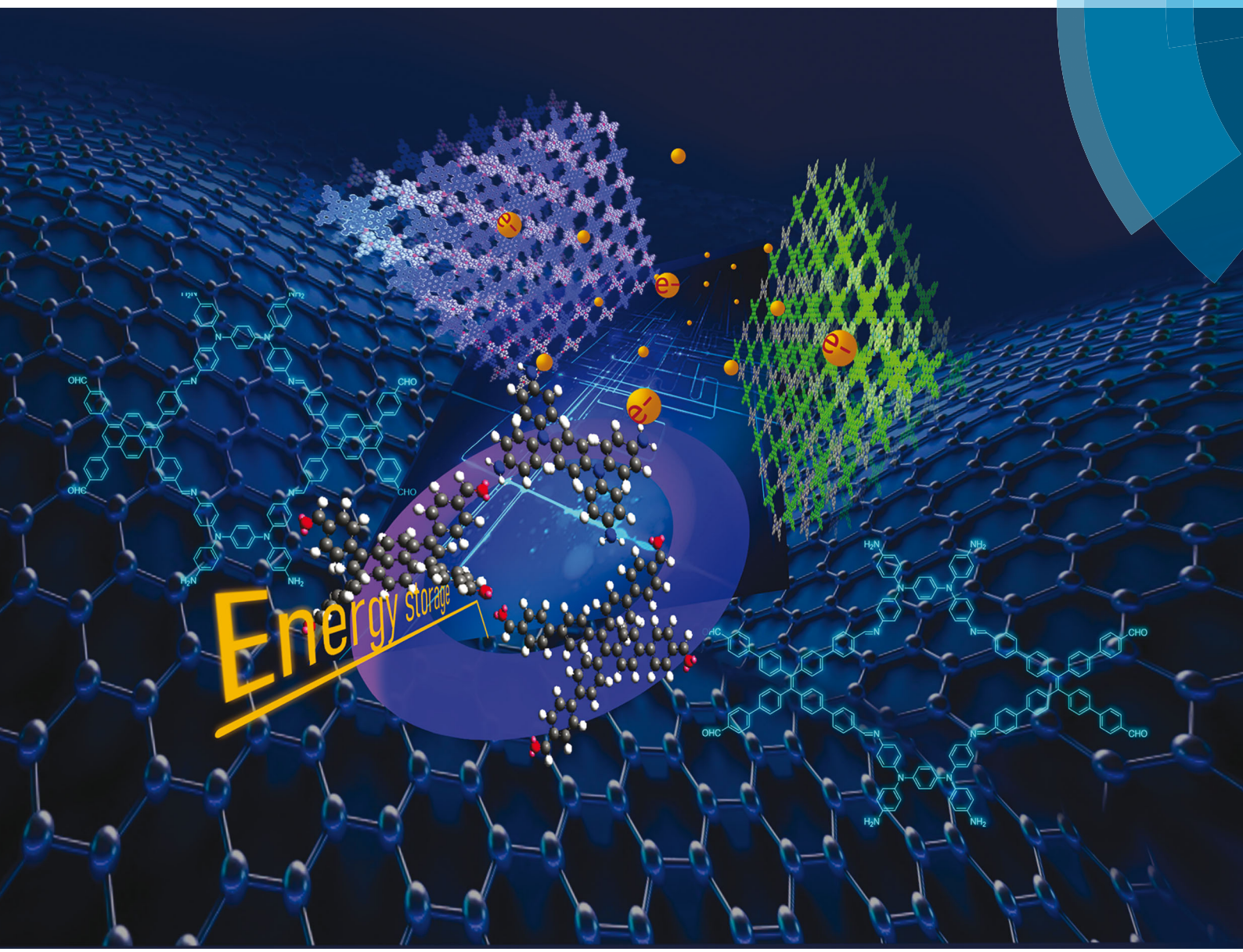

ISSN 1359-7345

ROYAL SOCIETY OF CHEMISTRY | Celebrating IYPT 2019

COMMUNICATION

Shiao-Wei Kuo *et al.*

Ultrastable tetraphenyl-*p*-phenylenediamine-based covalent organic frameworks as platforms for high-performance electrochemical supercapacitors

ChemComm

COMMUNICATION

View Article Online
View Journal | View Issue

Published on 18 November 2019. Downloaded by National Sun Yat Sen University on 3/23/2020 9:57:54 AM.

Check for updates

Cite this: *Chem. Commun.*, 2019, 55, 14890

Received 17th October 2019,
Accepted 18th November 2019

DOI: 10.1039/c9cc08107k

rsc.li/chemcomm

Ultrastable tetraphenyl-*p*-phenylenediamine-based covalent organic frameworks as platforms for high-performance electrochemical supercapacitors†

Ahmed F. M. EL-Mahdy,[ab] Mohamed Gamal Mohamed,[ab] Tharwat Hassan Mansoure,[bcd] Hsiao-Hua Yu,[cd] Tao Chen[e] and Shiao-Wei Kuo*[af]

In this study we synthesized two tetraphenyl-*p*-phenylenediamine-based covalent organic frameworks (TPPDA-TPPyr and TPPDA-TPTPE COFs) for potential use in high-performance electrochemical supercapacitors. This excellent performance arose from their structures containing redox-active triphenylamine derivatives and their high surface areas.

Supercapacitors are attracting interest as alternatives to batteries, because of their high stabilities, fast charge/discharge rates, high power densities, and lifetimes on the order of 10^5 cycles.[1] The nature of the faradaic and non-faradaic processes that occur inside the supercapacitors depends mainly on the electrode material.[2] Initially, active carbon was used as the electrode material; it is a highly porous material that is highly conductive and stable under various acidic and basic conditions. Nevertheless, active carbon can only store energy with double-layer capacitors; therefore, its performance is affected significantly by the nature of its pores. A large number of carbon pores might make them excessively small or inaccessible to accommodate solvated electrolyte ions. This behavior of active carbon limits the energy density achievable with active carbon-based supercapacitors.[3] Nitrogen-doped carbon materials have improved the productivity and efficiency of supercapacitors significantly through both heteroatom and pseudocapacitance effects.[4] Several organic materials---including conductive polymers (*e.g.*, polythiophene, polyaniline, and polyimide), carbonyl-based compounds, organosulfur compounds, and stable radical polymers[5–7]—have been developed recently as novel materials for use as extremely efficient supercapacitors, due to their structural diversity, high redox capacities, and environmental friendliness.[8] Triphenylamine (TPA) derivatives have also been considered for their redox-active behavior,[9] excellent electronic properties, and high charge mobilities.[10] In particular, polytriphenylamine derivatives have been employed as electrode materials for energy storage in various kinds of supercapacitors, due to their excellent electroluminescence and charge transport properties, in addition to their excellent morphological and thermal stabilities.[11] Moreover, the polytriphenylamine skeleton containing TPA moieties as repeat radical units can undergo reversible radical redox processes during the charging and discharging processes.[12] Accordingly TPA derivatives are attractive materials for creating new conductively and electrochemically stable frameworks with high surface areas and controllable pore sizes for streamlining the rates of diffusion of solvent and electrolyte molecules.

Covalent organic frameworks (COFs) are designable crystalline networks having long-range periodic three- (3D) and two-dimensional (2D) structures that are precisely assembled through the cross-linking of organic building blocks through covalent bonds. Benefitting from their ordered pore sizes, high surface areas, and excellent crystallinity, dozens of COFs have been synthesized in recent years, with promising applications in, for example, energy storage, catalysis, gas storage, optoelectronics, drug delivery, and separation.[13–18] With respect to electrochemistry, COFs can exhibit distinct advantages over non-crystalline polymers, because of their controllable pore sizes and the ability to add redox-active moieties into their frameworks by varying their building blocks. Although a few COFs have been tested recently as electrode materials,[19] the number of redox-active moieties inserted into COF frameworks for use as new electrode materials has remained limited. To the

[a] *Department of Materials and Optoelectronic Science, Center of Crystal Research, National Sun Yat-Sen University, Kaohsiung 80424, Taiwan. E-mail: kuosw@faculty.nsysu.edu.tw*
[b] *Chemistry Department, Faculty of Science, Assiut University, Assiut 71516, Egypt*
[c] *Institute of Chemistry, Academia Sinica, 128 Academia Road Sec. 2, Nankang, Taipei 115, Taiwan*
[d] *Department of Chemistry and Nanoscience and Technology Program, Taiwan International Graduate Program, Academia Sinica and National Taiwan University, Taipei 106, Taiwan*
[e] *Ningbo Institute of Material Technology and Engineering, Chinese Academy of Science, Zhongguan West Road 1219, 315201 Ningbo, China*
[f] *Department of Medicinal and Applied Chemistry, Kaohsiung Medical University, Kaohsiung 807, Taiwan*

† Electronic supplementary information (ESI) available. See DOI: 10.1039/c9cc08107k

This journal is © The Royal Society of Chemistry 2019

Published on 18 November 2019. Downloaded by National Sun Yat Sen University on 3/23/2020 9:57:54 AM.

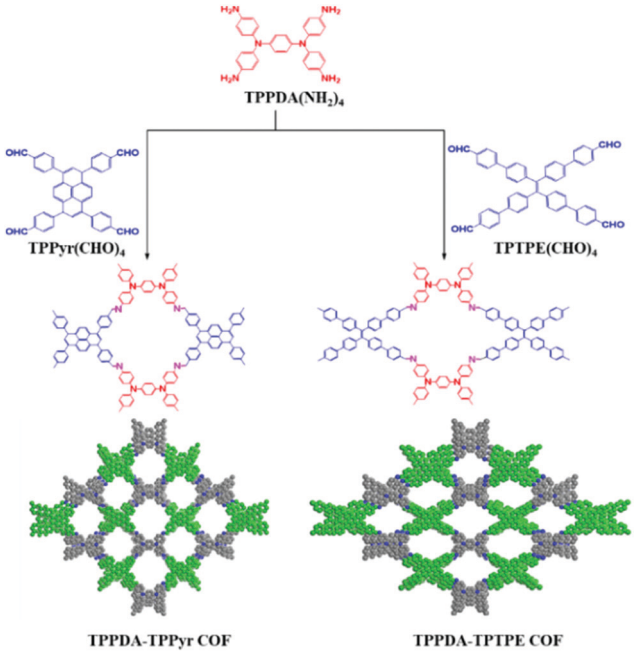

Scheme 1 Synthesis of **TPPDA-TPPyr** and **TPPDA-TPTPE COF**s.

best of our knowledge, tetraphenyl-*p*-phenylenediamine (TPPDA)-based COFs have not been reported previously. In this paper, we describe the synthesis of TPPDA-COFs through one-pot [4+4] Schiff-base condensations of redox-active **TPPDA(NH$_2$)$_4$** with tetraformyl linkers, **TPPyr(CHO)$_4$** and **TPTPE(CHO)$_4$** (Scheme 1).

To construct new imine-linked COFs featuring many triphenylamine moieties in their backbones, we prepared the new tetraamine precursor TPPDA(4NH$_2$) from *p*-phenylenediamine in two steps (Scheme S1, ESI†). The FTIR spectrum featured multiple signals 3456–3334 cm^{-1} for the symmetric and asymmetric NH groups (Fig. 1a and Fig. S1, ESI†). The ^{1}H NMR spectrum contained a broad singlet at 4.81 ppm, attributable to the four amino groups, as well as signals for the protons of the amino-substituted aromatic units in the range 6.68–6.46 ppm (Fig. S2, ESI†). The ^{13}C NMR spectrum of TPPDA(4NH$_2$) displayed a characteristic signal at 145.17 ppm for the C–NH$_2$ nuclei, in addition to signals for the other aromatic carbon nuclei at 142.57, 138.05, 126.49, 120.96, and 115.44 ppm (Fig. 1b and Fig. S3, ESI†). We obtained organic crystallites of the **TPPDA-TPPyr** and **TPPDA-TPTPE COF**s after solvothermic condensations of TPPDA(4NH$_2$) with **TPPyr(CHO)$_4$** and **TPTPE(CHO)$_4$**, respectively. The FTIR spectra of the **TPPDA-TPPyr** and **TPPDA-TPTPE COF**s featured intense signals at 1622 and 1624 cm^{-1}, respectively, corresponding to their imine (C═N) stretching vibrations (Fig. 1a and Fig. S4, S5, ESI†). The intensities of the bands corresponding to the amino NH and formyl CHO stretching vibrations of TPPDA(4NH$_2$) and **TPPyr(CHO)$_4$/TPTPE(CHO)$_4$**, respectively, were significantly attenuated (Fig. 1a and Fig. S4, S5, ESI†), implying a great degree of imine-linkage formation. The chemical structures of the **TPPDA-TPPyr** and **TPPDA-TPTPE COF**s were confirmed using solid state NMR spectroscopy (Fig. 1b and Fig. S6, S7, ESI†). The ^{13}C solid state NMR spectra of the synthesized COFs featured signals at 178.43–179.79 ppm for the imino-carbon (C═N) nuclei, but the signals of the C–NH$_2$ and CHO carbon nuclei of the tetraamine and tetraformyl precursors were absent. Thermogravimetric analysis (TGA) of the **TPPDA-TPPyr** and **TPPDA-TPTPE COF**s revealed their extraordinary thermal stability, with values of T_{d10} of approximately 543 and 551 °C, respectively, and char yields of 70 and 68 wt%, respectively (Fig. S8 and Table S1, ESI†). Thus, the thermal stabilities of these COFs are superior to those of most previously reported 2D COFs, whose decomposition temperatures have typically been below 350 °C.

TEM images of the **TPPDA-TPPyr COF** suggested the presence of ordered and porous nanofibers, with lengths of up to several micrometers and diameters of 150–400 nm (Fig. 1c and Fig. S9, ESI†); TEM images of the **TPPDA-TPTPE COF** revealed fan

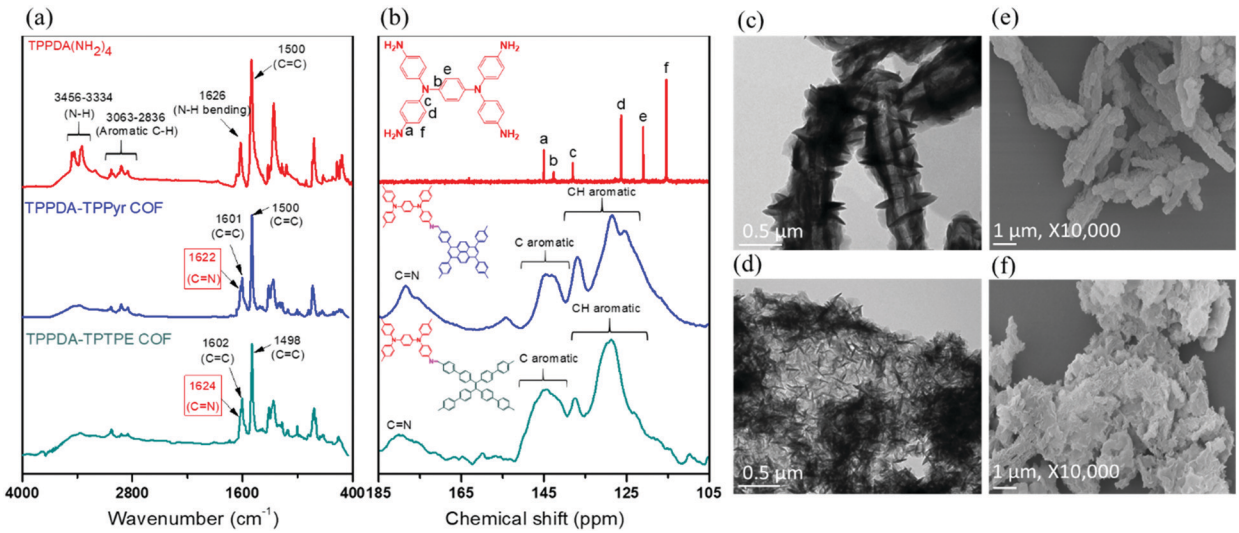

Fig. 1 (a) FTIR and (b) solid state ^{13}C NMR spectra of **TPPDA(NH$_2$)$_4$** (red), **TPPDA-TPPyr** (blue), and **TPPDA-TPTPE COF**s (green). (c and d) TEM and (e and f) FE-SEM images of the (c and e) **TPPDA-TPPyr** and (d and f) **TPPDA-TPTPE COF**s.

Published on 18 November 2019. Downloaded by National Sun Yat Sen University on 3/23/2020 9:57:54 AM.

blade-like crystallites with lengths of up to several nanometers and diameters of 40–80 nm (Fig. 1d and Fig. S10, ESI†). The FE-SEM images confirmed the nanofiber and fan blade-like morphologies of the **TPPDA-TPPyr** and **TPPDA-TPTPE COFs**, respectively (Fig. 1e, f, and Fig. S11, ESI†).

To gain insight into the crystallinities of the **TPPDA-TPPyr** and **TPPDA-TPTPE COFs**, we recorded their powder X-ray diffraction (PXRD) patterns (Fig. 2a and b), which revealed that the **TPPDA-TPPyr** and **TPPDA-TPTPE COFs** both possessed microcrystalline frameworks with long-ordered structures. In Fig. 2a, the experimental PXRD (red curve) of the **TPPDA-TPPyr COF** featured an intense signal at 5.30°, which we assign to the 110 facet, in addition to a set of signals at 10.60°, 11.88°, and 16.07°, assignable to the diffractions of the 210, 220, and 310 facets, respectively. We attribute the broad diffraction signal at 20.83° to the 001 facet, which appeared because of strong π-stacking between the tetragonal 2D interlayers of the **TPPDA-TPPyr COF** (Fig. 2a). Similarly, the PXRD pattern of the **TPPDA-TPTPE COF** featured an intense signal at 4.95°, corresponding to the 110 facet, as well as other characteristic signals at 9.94°, 12.07°, 14.89°, and 20.30°, assigned to the diffractions of the 210, 220, 310, and 001 facets, respectively (Fig. 2b). We applied the Bragg equation to calculate the 2D *d*-spacing between the 100 planes (d_{100}) and the 2D π-interlayer distance between the COF stacked sheets. The values of d_{100} of the **TPPDA-TPPyr** and **TPPDA-TPTPE COFs** were 1.66 and 1.78 nm, respectively, while their π-stacking distances were 4.2 and 4.4 Å, respectively (Table S2, ESI†). The hypothetical PXRD patterns of the **TPPDA-TPPyr** and **TPPDA-TPTPE COFs** (Fig. 2a and b, green curves), obtained from the Pawley refinements, were consistent with the experimental patterns (Fig. 2a and b, red curves), with only very small differences (Fig. 2a and b, black curves).

To further study the conformations and unit cell parameters of our synthesized **TPPDA-TPPyr** and **TPPDA-TPTPE COFs**, we used Material Studio software to construct appropriate AA and AB stacking models. The resulting data confirmed that the experimental PXRD patterns strongly matched the simulated ones for the corresponding AA stacking models (Fig. 2a, b and Fig. S12, S13, blue curves, ESI†), but they contrasted for the AB stacking models (Fig. 2a and b, purple curves). We obtained the following parameters for the unit cells of the AA stacking models: for **TPPDA-TPPyr COF**, a = 23.72 Å, b = 23.98 Å, c = 4.51 Å, α = 104.69°, β = 91.46°, γ = 90.11° (Fig. S14, S15 and Table S3, ESI†); for **TPPDA-TPTPE COF**, a = 30.17 Å, b = 22.29 Å, c = 5.02 Å, α = 82.62°, β = 86.04°, γ = 90.06° (Fig. S16, S17 and Table S4, ESI†). We recorded N_2 adsorption/desorption isotherms of our synthesized **TPPDA-TPPyr** and **TPPDA-TPTPE COFs** at 77 K to assess the porosities of their COF frameworks (Fig. 2c). Their sorption curves revealed a hybrid of type I- and IV-isotherms with sharp uptakes at low pressure of $P/P_0 < 0.01$ for **TPPDA-TPPyr** and **TPPDA-TPTPE COFs** and hysteresis loops at high pressure of $P/P_0 > 0.2$ for **TPPDA-TPPyr COF** and at $P/P_0 > 0.1$ for **TPPDA-TPTPE COF**, indicating the presence of permanent micropores and mesopores. The presence of a mixture of micropores and mesoporous in electrode materials strongly enhanced the ion transport and diffusion pathway in the charge/discharge process.[20] Derived from the N_2 sorption isotherms, the Brunauer–Emmett–Teller (BET) surface areas of the **TPPDA-TPPyr** and **TPPDA-TPTPE COFs** were 1020 and 1067 $m^2\ g^{-1}$, respectively, and their pore volumes were 0.66 and 0.84 $cm^3\ g^{-1}$, respectively (Table S2, ESI†). Moreover, we used non-local density functional theory (DFT) to obtain the pore size distribution profiles of our synthesized COFs. The pore size distributions featured pore widths concentrated at 1.25 and 1.57 nm for the **TPPDA-TPPyr** and **TPPDA-TPTPE COFs**, respectively (Fig. 2d and Table S2, ESI†).

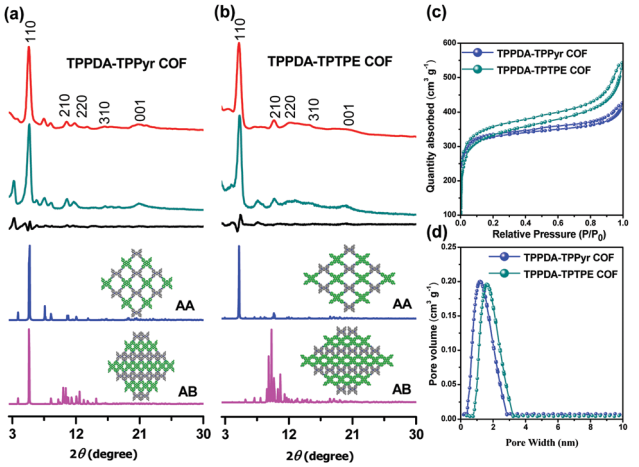

Fig. 2 (a and b) PXRD patterns of the (a) **TPPDA-TPPyr** and (b) **TPPDA-TPTPE COFs**: experimental patterns (red); simulated Pawley refined patterns (green); differences between the observed and simulated patterns (black); and AA (blue) and AB (purple) stacking patterns. (c) Nitrogen adsorption/desorption isotherms at 77 K and (d) pore size distributions for the **TPPDA-TPPyr** and **TPPDA-TPTPE COFs**.

We used cyclic voltammetry (CV) and the galvanostatic charge–discharge (GCD) method to examine the electrochemical performances of our TPPDA-COFs in a three-electrode system with 1 M KOH as the aqueous electrolyte. Fig. 3a and b display the corresponding CV curves of **TPPDA-TPPyr** and **TPPDA-TPTPE COFs**, recorded at various sweep rates from 5 to 200 mV s^{-1} in the potential window from +0.18 to −0.92 V. The **TPPDA-TPTPE COF** provided the relatively higher current density. The corresponding CV curves of these two COF samples had rectangle-like shapes featuring humps, indicating that this capacitive response originated from electric double-layer capacitance. The distinct appearance of humps in the rectangle-like shape is an indication of pseudocapacitance arising from the presence of the heteroatoms (*i.e.*, N atoms).[1,15,16] In addition, both samples possessed redox-active triphenylamine units,[15,16] which allowed them to undergo reversible redox processes at a low sweep rate (5 mV s^{-1}) in the potential window from +0.18 to −0.92 V (Fig. S18, ESI†). As previously reported, triphenylamine possesses nitrogen electroactive center connected to three electron-rich phenyl rings, in which a reversible radical redox process occurs during charge and discharge processes.[9] Moreover, the current density increased upon increasing the sweep rate, while the shape of the CV curve was retained (Fig. 3a and b), indicating good rate capability and facile kinetics.[21,22] Fig. 3c and d present the GCD

 This journal is © The Royal Society of Chemistry 2019

Published on 18 November 2019. Downloaded by National Sun Yat Sen University on 3/23/2020 9:57:54 AM.

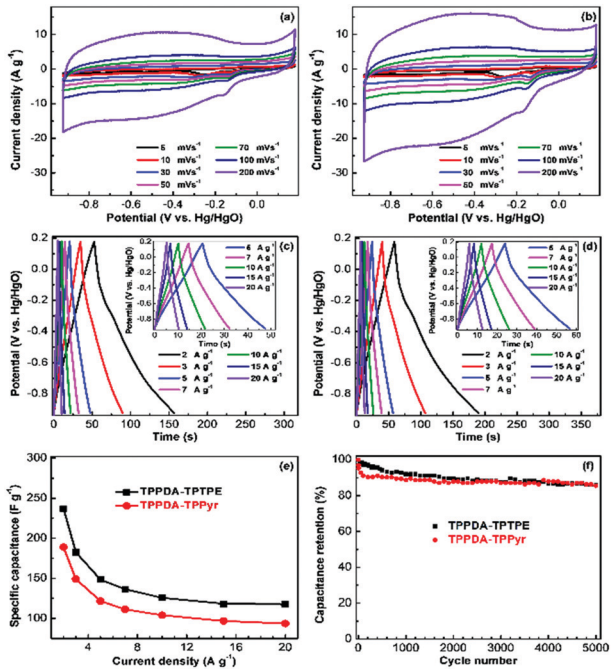

Fig. 3 (a and b) CV and (c and d) GCD profiles, recorded in 1 M KOH, of the (a and c) **TPPDA-TPPyr** and (b and d) **TPPDA-TPTPE COF**s. (e) Corresponding specific capacitances determined at various current densities. (f) Cycling performance measured at a current density of 10 A g^{-1} for 5000 cycles.

curves of the **TPPDA-TPPyr** and **TPPDA-TPTPE COF**s measured at various current densities from 2 to 20 A g^{-1}. These GCD curves had triangular shapes featuring a slight bend, suggesting both pseudocapacity and EDLC characteristics.[13] The discharging time of the **TPPDA-TPTPE COF** was longer than that of the **TPPDA-TPPyr COF** (Fig. 3c and d), indicating that the capacitance of the former was larger than that of the latter. We used eqn (S1) (ESI†) to determine the specific capacitances from the GCD curves (Fig. 3e). The specific capacitance of the **TPPDA-TPTPE COF** (237.1 F g^{-1}) was larger than that of the **TPPDA-TPPyr COF** (188.7 F g^{-1}) at a current density of 2 A g^{-1}. This excellent performance of the **TPPDA-TPTPE COF** was due to its higher surface area (1067 m^2 g^{-1}) and pore volume (0.84 cm^3 g^{-1}), along with its heteroatoms, all of which made it easier for the electrolytes to access the surface of the electrode.[21] Table S5 (ESI†) summarizes the corresponding surface areas and specific capacitances. We examined the durability of our TPPDA-COFs by cycling them over 5000 times at 10 A g^{-1} (Fig. 3f). These two **TPPDA-TPTPE** and **TPPDA-TPPyr COF**s displayed excellent cycling stability, with 86.2 and 85.6% retention, respectively, of their original capacitances after 5000 cycles. Comparing with reported stable electrode materials such as metal oxides[23] and MOF-derived metal oxides,[24] our TPPDA-COFs are among the highest stable electrodes. These high stabilities might be originated from the extraordinary thermal stability and excellent crystallinity of our COFs materials. The related Ragone plot (Fig. S19, ESI†) suggested that these two TPPDA-COFs electrodes possessed good energy and power densities.

In summary, we have prepared a novel redox-active triphenylamine derivative **TPPDA(NH_2)$_4$** and then used it in the synthesis of two TPPDA-COFs—**TPPDA-TPPyr** and **TPPDA-TPTPE COF**s—through [4+4] condensation of **TPPDA(NH_2)$_4$** with tetraformyl linkers. The resultant TPPDA-COFs had excellent crystallinities, extraordinary thermal stabilities and high surface areas. In addition, the TPPDA-COFs had excellent electrochemical capacitances because their chemical structures contained redox-active triphenylamine units. Moreover, the two **TPPDA-TPTPE** and **TPPDA-TPPyr COF**s displayed excellent cycling stability at 10 A g^{-1}, with 86.2 and 85.6% retention, respectively, of their original capacitances after 5000 cycles. We surmise that the massive stabilities of TPPDA-COFs possessing TPPDA redox-active moieties might be promising materials for high-performance real supercapacitors in several fields, particularly electrochemical energy storage devices.

Conflicts of interest

There are no conflicts to declare.

Notes and references

1 Z. Yu, L. Tetard, L. Zhai and J. Thomas, *Energy Environ. Sci.*, 2015, **8**, 702.
2 G. Wang, L. Zhang and J. Zhang, *Chem. Soc. Rev.*, 2012, **41**, 797S.
3 M. Sevilla and R. Mokaya, *Energy Environ. Sci.*, 2014, **7**, 1250.
4 D. Yang, Y. Song, Y. J. Ye, M. Zhang, X. Sun and X. X. Liu, *J. Mater. Chem. A*, 2019, **7**, 12086.
5 Z. P. Song, H. Zhan and Y. H. Zhou, *Angew. Chem., Int. Ed.*, 2010, **49**, 8444.
6 X. Han, C. Chang, L. Yuan, T. Sun and J. Sun, *Adv. Mater.*, 2007, **19**, 1616.
7 (*a*) J. Wang, Y. Lee, K. Tee, S. N. Riduan and Y. Zhang, *Chem. Commun.*, 2018, **54**, 7681; (*b*) Y. Sun, Y. Sun, Q. Pan, G. Li, B. Han, D. Zeng, Y. Zhang and H. Cheng, *Chem. Commun.*, 2016, **52**, 3000.
8 J. M. Moon, N. Thapliyal, K. K. Hussain, R. N. Goyal and Y. B. Shim, *Biosens. Bioelectron.*, 2018, **102**, 540.
9 C. Su, H. He, L. Xu, K. Zhao, C. Zheng and C. Zhang, *J. Mater. Chem. A*, 2017, **5**, 2701.
10 (*a*) A. F. M. El-Mahdy and S.-W. Kuo, *RSC Adv.*, 2018, **8**, 15266; (*b*) A. F. M. El-Mahdy and S.-W. Kuo, *Polymer*, 2018, **15**, 10.
11 R. Kabe and C. Adachi, *Nature*, 2017, **550**, 384.
12 A. Petr, C. Kvarnstrom, L. Dunsch and A. Ivaska, *Synth. Met.*, 2000, **108**, 245.
13 A. F. M. El-Mahdy, Y.-H. Hung, T. H. Mansoure, H.-H. Yu, T. Chen and S.-W. Kuo, *Chem. – Asian J.*, 2019, **14**, 1429.
14 S. Lin, C. S. Diercks, Y. B. Zhang, N. Kornienko, E. M. Nichols, Y. B. Zhao, A. R. Paris, D. Kim, P. Yang, O. M. Yaghi and C. J. Chang, *Science*, 2015, **349**, 1208–1213.
15 A. F. M. El-Mahdy, C.-H. Kuo, A. A. Alshehri, J. Kim, C. Young, Y. Yamauchi and S.-W. Kuo, *J. Mater. Chem. A*, 2018, **6**, 19532.
16 A. F. M. EL-Mahdy, C. Young, J. Kim, J. You, Y. Yamauchi and S.-W. Kuo, *ACS Appl. Mater. Interfaces*, 2019, **11**, 9343.
17 H. Wei, S. Z. Chai, N. T. Hu, Z. Yang, L. M. Wei and L. Wang, *Chem. Commun.*, 2015, **51**, 12178.
18 L. Bai, S. Z. F. Phua, W. Q. Lim, A. Jana, Z. Luo, H. P. Tham, L. Zhao, Q. Gao and Y. Zhao, *Chem. Commun.*, 2016, **52**, 4128.
19 C. R. DeBlase, K. E. Silberstein, T.-T. Truong, H. D. Abruña and W. R. Dichtel, *J. Am. Chem. Soc.*, 2013, **135**, 16821.
20 (*a*) D. Chen, L. Li, Y. Xi, J. Li, M. Lu, J. Cao and W. Han, *Electrochim. Acta*, 2018, **286**, 264; (*b*) M. Lu, L. Li, S. Shen, D. Chen and W. Han, *New J. Chem.*, 2019, **43**, 1032; (*c*) D. Chen, M. Lu, L. Li, D. Cai, J. Li, J. Cao and W. Han, *J. Mater. Chem. A*, 2019, **7**, 21759.
21 F. Hu, J. Wang, S. Hu, L. Li, W. Shao, J. Qiu, Z. Lei, W. Deng and X. Jian, *ACS Appl. Mater. Interfaces*, 2017, **9**, 31940.
22 A. M. Khattak, Z. A. Ghazi, B. Liang, N. A. Khan, A. Iqbal, L. Li and Z. Tang, *J. Mater. Chem. A*, 2016, **4**, 16312.
23 (*a*) X. Xia, S. Deng, D. Xie, Y. Wang, S. Feng, J. Wu and J. Tu, *J. Mater. Chem. A*, 2018, **6**, 15546–15552; (*b*) X. Xia, S. Deng, S. Feng, J. Wu and J. Tu, *J. Mater. Chem. A*, 2017, **5**, 21134.
24 (*a*) R. R. Salunkhe, Y. V. Kaneti and Y. Yamauchi, *ACS Nano*, 2017, **11**, 5293; (*b*) R. R. Salunkhe, J. Tang, N. Kobayashi, J. Kim, Y. Ide, S. Tominaka, J. H. Kim and Y. Yamauchi, *Chem. Sci.*, 2016, **7**, 5704; (*c*) C. Young, J. Wang, J. Kim, Y. Sugahara, J. Henzie and Y. Yamauchi, *Chem. Mater.*, 2018, **30**, 3379.